Designing Globally Time-Optimal Entangling Gates Using Geometric Space Curves

Ho Lun Tang,[1,2,*] Kyle Connelly,[1,2] Ada Warren,[1,2] Fei Zhuang,[1,2] Sophia E. Economou,[1,2] and Edwin Barnes[1,2]

[1] *Department of Physics, Virginia Tech, Blacksburg, Virginia 24061, USA*

[2] *Virginia Tech Center for Quantum Information Science and Engineering, Blacksburg, Virginia 24061, USA*

(Received 3 May 2022; revised 8 March 2023; accepted 29 March 2023; published 28 April 2023)

High-fidelity entangling gates are essential for quantum computation. Currently, most approaches to designing such gates are based either on simple, analytical pulse waveforms or on ones obtained from numerical optimization techniques. In both cases, it is typically not possible to obtain a global understanding of the space of waveforms that generate a target gate operation, which can make it challenging to identify globally time-optimal waveforms that respect amplitude and bandwidth constraints. Here, we show that in the case of weakly coupled qubits, it is possible to find all pulses that implement a target entangling gate in near-minimal time. We do this by mapping quantum evolution onto geometric space curves. We derive the minimal conditions these curves must satisfy in order to guarantee a gate with a desired entangling power is implemented. Pulse waveforms are extracted from the curvatures of these curves. We illustrate our method by designing fast, CNOT-equivalent entangling gates for silicon quantum dot spin qubits with fidelities exceeding 99 %. We show that fidelities can be further improved while maintaining low bandwidth requirements by using geometrically derived pulses as initial guesses in numerical optimization routines.

DOI: 10.1103/PhysRevApplied.19.044094

I. INTRODUCTION

High-fidelity entangling gates are a key requirement in all circuit-based approaches to quantum computing. Such gates are often implemented using electromagnetic pulse waveforms based on simple analytical shapes such as square or Gaussian functions, with fidelities optimized by adjusting amplitudes, timings, or bandwidths [1–6]. Numerical pulse-shape optimization recipes such as gradient-ascent pulse engineering (GRAPE) or chopped random basis (CRAB) are also commonly employed to improve fidelities further [6–13]. Such methods have led to experimental demonstrations of high-fidelity entangling gates in silicon quantum dots [14–20], superconducting qubits [21–25], and trapped ions [26–28].

Despite the substantial progress that has been made in recent years, further improvements in entangling gates are still widely needed. In addition to the very high fidelities that are required to comfortably exceed error-correction thresholds [29,30], it is also useful to reduce gate times and pulse amplitude and bandwidth requirements as much as possible to speed up algorithms and lessen the technological overhead. Finding pulse waveforms that are optimal with respect to all these factors is generally a challenging task. While numerical techniques address this issue to a large extent, it is often still difficult to obtain globally time-optimal solutions with numerical methods alone. This motivates the search for complementary methods that provide a global, analytical understanding of the space of pulse waveforms that generate a target gate operation. Such methods, in combination with numerical optimization protocols, could lead to significant enhancements in gate performance.

Recently, it has been shown that there exists a correspondence between quantum evolution and geometric space curves [31]. This connection provides a global perspective on the relationship between pulses and the quantum evolution they generate through a formalism called space-curve quantum control (SCQC). This has been exploited to design single- and two-qubit gates that dynamically correct for noise that acts transversely to the driving field [32–35]. In SCQC, noise-resistant pulse waveforms are obtained from the geometric properties of closed space curves. This technique was also applied to study the speed limit of dynamically corrected gates [33], noise-resilient Landau-Zener transitions [36], and gates that are simultaneously robust against pulse errors and transverse noise [37,38].

*holuntang@vt.edu

 © 2023 American Physical Society

In this work, we show that entanglement growth in weakly coupled two-qubit systems can also be mapped to space curves. We use this mapping to develop a geometric framework for finding infinitely many pulses that generate a target entangling gate. Remarkably, we find that the net displacement of a space curve determines the entangling power of the resulting gate. The pulses that produce this entanglement can be obtained from the generalized curvatures of the curve. This provides a general method for finding pulses that implement gates with a target entangling power. Moreover, the arclength of the curve is equal to the gate time, providing a systematic way to find globally time-optimal pulses that create a desired amount of entanglement. We demonstrate this method in the context of silicon quantum dot spin qubits, where we derive the minimal space-curve conditions needed to produce CNOT-equivalent gates. We show that the pulses extracted from these curves generate maximally entangling gates with fidelities exceeding 99% and gate times below 30 ns for typical experimental parameters. We show that using these geometrically engineered pulses as a seed in numerical optimization routines can further improve the fidelities beyond what is achievable with random initial guesses. In this way, we can inject global information about the control landscape into numerical methods and thus help them avoid unnecessarily complicated pulse shapes and long gate times.

The paper is organized as follows. In Sec. II, we introduce the two-qubit silicon spin system example that we focus on throughout this work. In Sec. III, we present our geometric framework that relates two-qubit entanglement growth to space curves in three dimensions. We provide explicit examples of driving pulses and the corresponding high-fidelity entangling gates they generate. In Sec. IV A, we examine how the geometrically derived pulses perform after numerical optimization.

II. SPIN-QUBIT SYSTEM

Throughout this work, we focus on the case of silicon quantum dot spin qubits to illustrate our approach, although the basic idea can be applied to any weakly coupled qubit system. Single-electron spin qubits in silicon quantum dots are a promising platform for quantum computation, due to long coherence times, the availability of all-electrical control, and the potential for scalability afforded by the existing silicon manufacturing infrastructure [39–42]. While high-fidelity single- and two-qubit gates were demonstrated by several groups recently [15–18,43], further improvements in two-qubit gate fidelities are still needed for most error-correction schemes. The fidelity is mainly limited by charge noise and nuclear spin-bath fluctuations [44–46]. Since the natural abundance of the spinful isotope ^{29}Si is only 4.7 %, and can be further reduced by isotopic purification [47], charge noise is widely considered the dominant source of noise in the system.

The specific system we focus on consists of two electrons trapped in a silicon double quantum dot (DQD). We begin by deriving an effective Hamiltonian for this system following the analysis of Ref. [4]. In the following section, we use this effective Hamiltonian to establish the correspondence between two-qubit evolution and space curves. The two electron spins are subject to an external magnetic field from a micromagnet, which is designed to maximize dB_z/dx and dB_y/dz. The first term gives rise to the different Zeeman splittings of the two qubits since they are separated along the x axis, well separating the resonance frequencies of the two qubits. The strong gradient along the z axis, i.e., dB_y/dz, is designed for electric dipole spin resonance (EDSR) control [48]. By applying a microwave pulse to the metal gate, we can oscillate the position of the electrons primarily in the z axis, which leads to an oscillating B_y magnetic field as seen by the electron, enabling EDSR control. The exchange interaction between the two spins, $J(t)$, can be tuned by changing the energy barrier via a middle metal gate, which also controls the separation between the dots [49,50]. Our starting point is the Heisenberg Hamiltonian,

$$H(t) = J(t)\left(\vec{S}_L \cdot \vec{S}_R - \frac{1}{4}\right) + \vec{S}_L \cdot \vec{B}_L + \vec{S}_R \cdot \vec{B}_R, \qquad (1)$$

where $\vec{S}_L$ ($\vec{S}_R$) is the spin operator of the electron in the left (right) quantum dot. The external magnetic field $\vec{B}_{L,R}$ has two components along the y and z axes. The y component is time dependent due to the drive field causing the electron oscillation in z direction, i.e., $B_{y,q} = B^0_{y,q} + B^1_{y,q}(t)\cos(\omega t + \phi)$, where $q = L/R$, ω, and ϕ are the driving frequency and phase, respectively. On the other hand, the z component of the magnetic field, which sets the Zeeman splitting of the two qubits, is kept constant throughout the control process. It is only slowly changed while the exchange coupling J is being turned on and off adiabatically, but in general, it is a function of the exchange coupling $B_{z,q}(J) = B^0_{z,q} + B^1_{z,q}(J)$, where the first term is the field when $J = 0$.

Following Ref. [4], we work with the eigenbasis set of the undriven version of the Hamiltonian in Eq. (1), i.e., $B_{y,q} = 0$, where the computational basis $|\uparrow\downarrow\rangle$ and $|\downarrow\uparrow\rangle$ are superposed into $|\widetilde{\uparrow\downarrow}\rangle$ and $|\widetilde{\downarrow\uparrow}\rangle$ by the exchange coupling. We then go to the interaction picture defined by the undriven and uncoupled Hamiltonian ($B_{y,q} = J = 0$). Together with the approximation justified by the larger Zeeman splitting deference between the two qubits compared to the exchange coupling, i.e., $J \ll |B_{z,L} - B_{z,R}|$, the interaction picture Hamiltonian becomes

$$H_{\text{int}} = \frac{1}{2}\begin{pmatrix} 2\bar{B}_z^1 & -i(B_{y,L}+\xi B_{y,R})e^{-i\alpha_- t} & -i(B_{y,R}-\xi B_{y,L})e^{i\alpha_+ t} & 0 \\ i(B_{y,L}+\xi B_{y,R})e^{i\alpha_- t} & \Delta B_z^1 - J + \frac{J\xi}{2} & 0 & -i(B_{y,R}+\xi B_{y,L})e^{i\alpha_+ t} \\ i(B_{y,R}-\xi B_{y,L})e^{-i\alpha_+ t} & 0 & -\Delta B_z^1 - J - \frac{J\xi}{2} & -i(B_{y,L}-\xi B_{y,R})e^{-i\alpha_- t} \\ 0 & i(B_{y,R}+\xi B_{y,L})e^{-i\alpha_+ t} & i(B_{y,L}-\xi B_{y,R})e^{i\alpha_- t} & -2\bar{B}_z^1 \end{pmatrix}, \quad (2)$$

where $\bar{B}_z = \left(B_{z,L}^0 + B_{z,R}^0\right)/2$, $\bar{B}_z^1 = \left(B_{z,L}^1 + B_{z,R}^1\right)/2$, $\Delta B_z = B_{z,R}^0 - B_{z,L}^0$, $\Delta B_z^1 = B_{z,R}^1 - B_{z,L}^1$, $\alpha_\pm = (\Delta B_z \pm 2\bar{B}_z)/2$, and $\xi = J/(\Delta B_z + \Delta B_z^1)$. This is the Hamiltonian used in the numerical calculations throughout this work, and we use the parameters reported in Ref. [51]: $J/2\pi = 19.7$ MHz, $B_{z,L}^0/2\pi = 18.287$ GHz, $B_{z,R}^0/2\pi = 18.501$ GHz, $B_{z,L}^1/2\pi = 52.71$ MHz, $B_{z,R}^1/2\pi = 5.76$ MHz, $B_{y,L}^0/2\pi = 5$ MHz, $B_{y,R}^0/2\pi = 55$ MHz, and $\phi = 3\pi/2$.

To gain a better understanding of the evolution generated by this Hamiltonian, it helps to further simplify the model by switching to a rotating frame, $H_{\text{rot}} = U_\omega H U_\omega^\dagger - iU_\omega \dot{U}_\omega^\dagger$, with $U_\omega = \exp\left[i\omega t\left(S_{z,R} + Sz, L/\hbar\right)\right]$, and applying the rotating-wave approximation. Since our target is to obtain a certain entangling gate up to local unitaries and the rotating frame evolution operator is only different from the interaction frame by local unitaries, the gate in both frames has the same entangling properties. By matching the driving frequency ω to the resonance frequency of the left qubit, the driving on the right qubit becomes negligible compared to the Zeeman splitting difference, $B_{y,R}^1 \ll \Delta B_z + \Delta B_z^1$. Ultimately, we obtain the simplified Hamiltonian:

$$H_{\text{rot}} = \frac{1}{4}\begin{pmatrix} 0 & B_{y,L}^1(t) & 0 & 0 \\ B_{y,L}^1(t) & 0 & 0 & 0 \\ 0 & 0 & -2J & B_{y,L}^1(t) \\ 0 & 0 & B_{y,L}^1(t) & 2J \end{pmatrix} \quad (3)$$

$$= \frac{J}{4}(ZZ - IZ) + \frac{B_{y,L}^1}{4} IX. \quad (4)$$

This describes two qubits coupled by a weak Ising interaction, and only the second qubit is driven. In the absence of an ac drive ($B_{y,L}^1 = 0$), we see that a two-qubit CZ gate can still be generated up to a local Z gate on the first qubit. However, a nontrivial ac pulse is necessary to generate other types of maximally entangling gates such as CNOT.

III. GEOMETRIC SPACE CURVES AND CORRESPONDING PULSES

In previous works that used the SCQC formalism to design pulses [31–37], the space curves represented the effect of noise errors on the quantum evolution. Specifically, the net displacement between the initial and final points of the curve quantified the usefulness of the first-order term in a perturbative expansion of the evolution operator in powers of the noise error. In this work, we also use geometric space curves, but instead of quantifying the error due to noise, the space curve here represents the entanglement generated during the evolution.

Following the Hamiltonian in Eq. (4), we define the single-qubit terms of the Hamiltonian as $H_0 = -J/(4)IZ + \Omega(t)/(4)IX$, where $\Omega(t) = B_{y,L}^1$ is the driving pulse. We then switch to the rotating frame defined by H_0 so that the two-qubit interaction term $J/(4)ZZ$ is isolated. Again this rotating frame transformation only involves local unitaries, and so has no effect on the entangling properties. The evolution operator in this frame has the form

$$\begin{aligned} \tilde{U} &= \mathcal{T}\exp\left[-i\frac{J}{4}\int dt U_0^\dagger ZZ U_0\right] \\ &\approx \exp\left[-i\frac{J}{4}\int dt U_0^\dagger ZZ U_0\right] \\ &= \exp\left[-i\frac{J}{4}\left(R_1(t)ZX + R_2(t)ZY + R_3(t)ZZ\right)\right]. \end{aligned} \quad (5)$$

Here, we keep only the first-order term in the Magnus expansion of the evolution operator. The three components $\{R_1(t), R_2(t), R_3(t)\}$ define the coordinates of a three-dimensional (3D) space curve $\vec{R}(t)$ parameterized by evolution time t, i.e.,

$$\tilde{U} \approx \exp\left[-i\frac{J}{4} Z \otimes \left(\vec{R}(t)\cdot\vec{\sigma}\right)\right]. \quad (6)$$

In what follows, we see that truncating the Magnus expansion at first order allows us to obtain simple analytical conditions on the space curve that guarantee a desired entangling power is achieved in the resulting gate. Below, we see that this is sufficient to achieve very high gate fidelities for typical parameter values realized in spin-qubit experiments. One could also keep higher orders of the Magnus expansion in Eq. (5), which would result in more complicated expressions for the Makhlin invariants in terms of $\vec{R}(t)$. As an example, we show the resulting expressions up to second order in Appendix A. Including these corrections would allow one to enforce a target entangling power to still greater accuracy.

A. Makhlin invariants

In order to study the entangling properties of this two-qubit gate, we consider the Makhlin invariants introduced in Ref. [52]:

$$G_1 = \frac{[\mathrm{Tr}(M)]^2}{16 \det U}, \tag{7}$$

$$G_2 = \frac{[\mathrm{Tr}(M)]^2 - \mathrm{Tr}(M^2)}{4 \det U}, \tag{8}$$

where U is a two-qubit unitary, and M is its symmetrized version expressed in the Bell basis:

$$M = \left(Q^\dagger U Q\right)^T \left(Q^\dagger U Q\right), \tag{9}$$

$$Q = \frac{1}{\sqrt{2}} \begin{pmatrix} 1 & 0 & 0 & i \\ 0 & i & 1 & 0 \\ 0 & i & -1 & 0 \\ 1 & 0 & 0 & -i \end{pmatrix}. \tag{10}$$

These two quantities are invariant under local operations so that they encode only the entanglement information, and any two-qubit unitaries with the same Makhlin invariants are equivalent up to local operations. Here, we aim to design two-qubit entangling gates with specified Makhlin invariants.

Using the fact that $QQ^T = -YY$, the trace of M can be rewritten as

$$\mathrm{Tr}(M) = \mathrm{Tr}\left(YYU^T YYU\right). \tag{11}$$

We further exploit the fact that the symmetric two-qubit Pauli terms in Eq. (6) commute with YY, while the antisymmetric term anticommutes with YY, therefore $YY\tilde{U}^T YY = \tilde{U}$. The trace of M can be further simplified

$$\mathrm{Tr}\,(M) = \mathrm{Tr}\left(\tilde{U}^2\right) = 4\cos\left(\frac{J}{2}|\vec{R}|\right), \tag{12}$$

$$\mathrm{Tr}\left(M^2\right) = \mathrm{Tr}\left(\tilde{U}^4\right) = 4\cos\left(J|\vec{R}|\right). \tag{13}$$

The corresponding Makhlin invariants read as

$$G_1 = \cos^2\left(\frac{J}{2}|\vec{R}|\right), \tag{14}$$

$$G_2 = 2 + \cos\left(J|\vec{R}|\right). \tag{15}$$

Of note, we see that the entangling power of the pulse is governed solely by the net displacement between the initial and final points of the space curve. For example, we can see that at $t = 0$, $\vec{R}(0) = 0$, and hence $G_1 = 1$ and $G_2 = 3$, which correspond to the identity operation. When $J|\vec{R}| = (2n+1)\pi$, we have $G_1 = 0$ and $G_2 = 1$, which correspond to a CNOT-equivalent gate. Generally the Makhlin invariants for a conditional X rotation $R_X(\theta)$ are

$$G_1 = \cos^2(\theta), \tag{16}$$

$$G_2 = 2 + \cos(2\theta), \tag{17}$$

and thus one can obtain a controlled $R_X(\theta)$ for any arbitrary angle by tuning the final displacement $|\vec{R}(t_f)|$.

The fact that only the net displacement matters in determining the entangling power of the pulse not only makes it simple to find pulses that generate a desired amount of entanglement, but it also reveals how we can obtain globally time-optimal entangling gates: because the gate time equals the arclength of the curve, pulses that implement time-optimal gates can be obtained by constructing minimal-length curves that satisfy the appropriate net displacement. A similar observation was made in Ref. [33] in the context of dynamically corrected gates, where globally time-optimal pulses were obtained by finding closed minimal-length curves with bounded curvature. There, it was shown that the resulting time-optimal pulses are consistent with Pontryagin's maximum principle [53] in the sense that the optimal pulses saturate the chosen amplitude bounds at all times. Such pulses have a square waveform unless additional constraints are imposed, for example, on the pulse bandwidth.

In the present work, we obtain smooth, nearly time-optimal pulses by constructing smooth, "nearly straight" curves with the desired displacement. Of course, the shortest such curve is a straight line extending radially from the origin. We show below that this time-optimal solution corresponds to the case of no ac pulse ($\Omega(t) = 0$), in which case we obtain a CZ gate when the length of the curve is $|\vec{R}| = \pi/J$. Thus, other maximally entangling gates with $\Omega(t) \neq 0$ like CNOT necessarily take longer to implement, with gate times lower bounded by π/J, which is equal to 25.4 ns for the device parameters listed above.

B. Geometric properties of the space curve

After designing the 3D space curve $\vec{R}(t)$ with the desired final displacement, the corresponding driving pulse can be read from the geometric properties of the curve. The local curvature $\kappa(t)$ and torsion $\tau(t)$ can be obtained from time derivatives of $\vec{R}(t)$:

$$\kappa_R = \left|\ddot{\vec{R}}\right| = \frac{\Omega}{2}, \tag{18}$$

$$\tau_R = \frac{\left(\dot{\vec{R}} \times \ddot{\vec{R}}\right) \cdot \dddot{\vec{R}}}{\left|\dot{\vec{R}} \times \ddot{\vec{R}}\right|^2} = \frac{J}{2}. \tag{19}$$

We see that the driving pulse is equal to twice the curvature of the space curve, while the torsion is $J/2$. This means that all constant-torsion curves $\vec{R}(t)$ with $\tau_R = J/2$ and final displacement $|\vec{R}(t_f)|$ yield a pulse $\Omega(t) = 2\kappa_R$ that generates a controlled $R_X(\theta)$ gate with $\theta = J|\vec{R}(t_f)|/2$. One exception to this arises when the curve is a straight line, in which case $\kappa_R = 0 \Rightarrow \Omega(t) = 0$, which corresponds to a time-optimal CPhase gate as discussed above. Other types of two-qubit gates require nontrivial curves with varying curvature and constant torsion. To design a constant-torsion curve, we follow the approach of Ref. [36]. Consider the coordinate system defined by the three orthonormal vectors $\{\hat{T}, \hat{N}, \hat{B}\}$ associated with the curve, where $\hat{T} = \dot{\vec{R}}$ is the tangent vector, $\hat{N} = \dot{\hat{T}}/\left|\dot{\hat{T}}\right|$ is the normal vector, and $\hat{B}$ is the binormal vector, given by $\hat{B} = \hat{T} \times \hat{N}$. These vectors obey the Frenet-Serret equations,

$$\frac{d}{dt}\begin{pmatrix} \hat{T} \\ \hat{N} \\ \hat{B} \end{pmatrix} = \begin{pmatrix} 0 & \kappa_R & 0 \\ -\kappa_R & 0 & \tau_R \\ 0 & -\tau_R & 0 \end{pmatrix}\begin{pmatrix} \hat{T} \\ \hat{N} \\ \hat{B} \end{pmatrix}. \tag{20}$$

By manipulating the relation between $\{\hat{T}, \hat{N}, \hat{B}\}$, we find

$$\begin{aligned}\vec{R}(t) &= \int_0^t \hat{T}(t')dt' = \int_0^t \hat{N}(t') \times \hat{B}(t')dt' \\ &= -\int_0^t \frac{1}{\tau_R}\frac{d\hat{B}}{dt'} \times \hat{B}(t')dt' = \frac{1}{\tau_R}\int \hat{B} \times d\hat{B}.\end{aligned} \tag{21}$$

We can interpret $\hat{B}(t)$ as a curve in its own right. Thus, we see that starting from an arbitrary $\hat{B}(t)$ curve, which lies on a unit sphere, we can use this formula to find a space curve with constant torsion. Note that since $\left|\dot{\hat{B}}\right| = \left|-\tau_R \hat{N}\right| = \tau_R$, the arclength along the binormal curve is given by $\tau_R t$, and the curvature of the binormal curve is given by $\kappa_B = \left|d^2\hat{B}/d(\tau_R t)^2\right|$.

We would also like to find a driving pulse that starts and ends at zero amplitude, since these are typically easiest to implement in hardware. This property can be translated to the space-curve side by rewriting the curvature in terms of the TNB frame of the $\hat{B}$ curve:

$$\begin{aligned}\kappa_R &= \left|\frac{d\hat{T}}{dt}\right| = \left|\frac{d}{dt}\left(\frac{1}{\tau_R}\hat{B} \times \frac{d\hat{B}}{dt}\right)\right| = \tau_R\left|\hat{B} \times \frac{d^2\hat{B}}{d(\tau_R t)^2}\right| \\ &= \tau_R\kappa_B\left|\hat{B} \times \hat{N}_B\right| = \tau_R\kappa_B \sin\theta.\end{aligned} \tag{22}$$

Here θ denotes the angle between $\hat{B}$ and $\hat{N}_B$. Since $\hat{B}$ is a normal vector of the sphere, the term $\kappa_B \sin\theta$ can be recognized as the geodesic curvature of the binormal curve, $\kappa_{B,g}$, and the expression above becomes $\kappa_R/\tau_R = \kappa_{B,g}$. Thus in order for the pulse amplitude to start and end at zero, $\kappa_{B,g}$ must vanish at $t = 0$ and $t = t_f$. This is equivalent to requiring that $\hat{B}$ be parallel to $\hat{N}_B$ at $t = 0$ and $t = t_f$, or equivalently that $\hat{B}$ trace a great circle in infinitesimal neighborhoods around $t = 0$ and $t = t_f$.

C. Examples

To demonstrate the above method, we now show examples of space curves satisfying the conditions described above and their corresponding pulses. We use the following ansatz for the $\hat{B}$ curve:

$$\sqrt{1 - \lambda \sin^2 \beta l}\,(\cos l, \sin l, 0) + \sqrt{\lambda}\sin\beta l\,(0, 0, 1)\,, \tag{23}$$

where λ and β are parameters that can be tuned to achieve a desired value of $J|\vec{R}(t_f)|$, and l parameterizes the $\hat{B}$ curve, ranging from 0 to $l_f = \pi/\beta$. Here we choose specific values of β and perform a linear search for $\lambda \in [0, 1]$ to achieve $J|\vec{R}(t_f)| = (2n + 1)\pi$. This ansatz starts and ends as a great circle, which ensures that the corresponding pulse starts and ends at zero.

We obtain the corresponding pulse by first computing the space curve $\vec{R}(t)$ from $\hat{B}$ using Eq. (21) and then employing Eq. (18). We then numerically solve the Schrödinger equation with the full Hamiltonian in Eq. (2) to obtain the evolution operator U_{int}. Since the driving pulses are designed to create gates locally equivalent to a CNOT gate, we apply local unitaries before and after U_{int} to bring it as close as possible to a CNOT:

$$U = K_1 U_{\text{int}} K_2, \tag{24}$$

where the K_i are tensor products of single-qubit gates on both qubits, so each K_i depends on six rotation angles. The fidelity of U with a CNOT is then calculated using the formula

$$F = \frac{1}{n(n+1)}\left[\text{Tr}(U^\dagger U) + \left|\text{Tr}(U_{\text{targ}}^\dagger U)\right|^2\right], \tag{25}$$

where n is the Hilbert-space dimension, and U_{targ} is the target gate (i.e., a CNOT gate). The local unitaries K_i are chosen to maximize F. Figure 1 shows two examples of curves that yield CNOT gates up to local unitaries. Panels (a) and (b) show space curves $\vec{R}(t)$ generated from the $\hat{B}$ ansatz Eq. (23), with $J\left|\vec{R}(t_f)\right| = \pi$ and $J\left|\vec{R}(t_f)\right| = 3\pi$, respectively. Panels (c) and (d) then show the pulses derived from these space curves. These pulses achieve fidelities of 99.84% and 99.43 %, respectively.

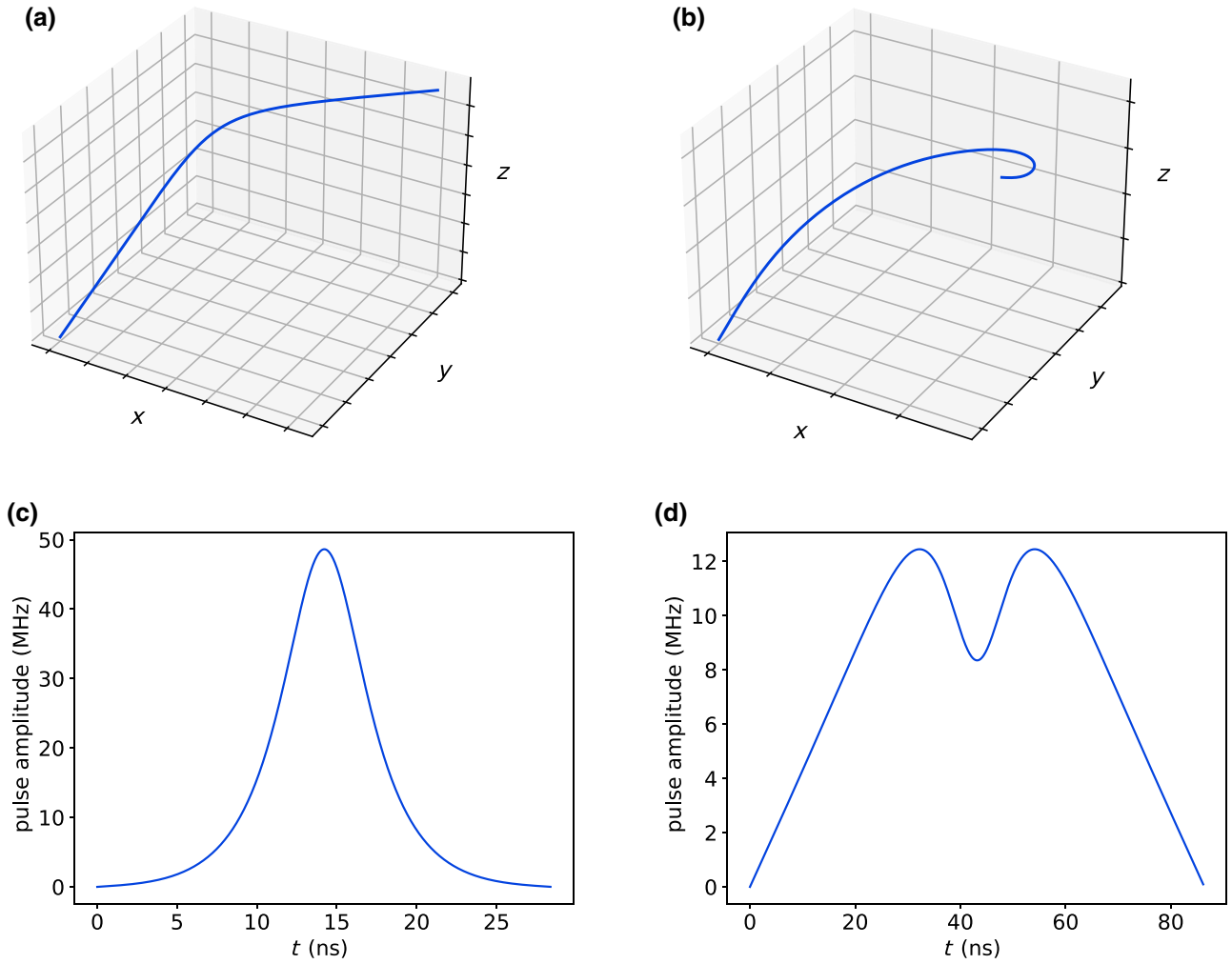

FIG. 1. (a) 3D space curve with $J|\vec{R}(t_f)| = \pi$, found by setting $\beta = 2\pi/3$ and $\lambda = 0.221163$. (b) 3D space curve with $J|\vec{R}(t_f)| = 3\pi$, found by setting $\beta = \pi/6$ and $\lambda = 0.561651$. (c) Corresponding driving pulse of (a) starts and ends at zero. It takes 28.3836 ns with fidelity 99.84 % by complementing the two-qubit gate with four single-qubit gates. (d) Corresponding driving pulse of curve in (b) with gate time 86.2373 ns and fidelity 99.43 %.

This fidelity could be further increased by taking into account higher-order terms in the Magnus expansion of $\tilde{U}$ in Eq. (5), which would give perturbative corrections to the driving pulse (see Appendix A). However, it is much simpler to use our first-order pulses as initial guesses for numerical optimization.

For comparison, we also ran simulations of our no-ac-pulse [$\Omega(t) = 0$] CZ gate, finding that the fidelity in this case is 1.80×10^{-8}.

IV. SPACE-CURVE PULSES AS THE INITIAL GUESS FOR NUMERICAL OPTIMIZATION

Although some optimal control theory problems may be solved exactly, in many realistic cases one must resort to finding a numerical solution to account for all of the details in the model or experiment. In this section, we numerically optimize our geometrically designed pulses using two widely used methods: GRAPE and CRAB. Our goal is to show that such methods benefit from using initial pulses obtained from the SCQC formalism, because such pulses are analytically guaranteed to be near a time-optimal solution. This in turn allows us to more easily constrain the shape of the optimized waveform to respect experimental bandwidth limitations. We illustrate this benefit by comparing our results to the gates that are obtained by instead inputting a random initial pulse into these numerical methods. In all examples considered, we find that using a geometrically designed pulse as the initial guess in numerical optimizers leads to simpler waveforms without sacrificing gate fidelity. In fact, in most cases, we also obtain significantly lower gate infidelities using the SCQC approach. These improved seed pulses and numerical optimization methods could be combined with characterization and calibration tools to yield further performance improvements in specific devices [54].

A. GRAPE

In quantum optimal control theory, one of the simplest and most popular numerical algorithms is GRAPE [7]. GRAPE works by discretizing the control pulse and then using a gradient ascent algorithm to find a pulse that maximizes the fidelity of U with some target gate U_{targ}. Specifically, to control a system with Hamiltonian $H(t) \equiv H_0 + \Omega(t)H_c$, the duration t_f of the pulse is broken up into N subintervals of length $\Delta t = t_f/N$, and $\Omega(t)$ is taken to be piecewise constant within each subinterval, $\Omega(t) = \Sigma_{k=0}^{N-1}\Omega_k\Theta(t - k\Delta t)\Theta((k+1)\Delta t - t)$. U is then approximated as

$$\begin{aligned} U &= U_{N-1}U_{N-2}\cdots U_1U_0, \\ U_k &= \exp(-i\Delta t(H_0 + \Omega_k H_c)). \end{aligned} \tag{26}$$

GRAPE then treats the pulse amplitudes Ω_k as free parameters, and numerically searches for values that maximize the fidelity of U with U_{targ} [Eq. (25)]. This can be done using a gradient ascent optimization, using the chain rule along with $\frac{\partial U}{\partial \Omega_k} \approx -i\Delta t U_{N-1}\cdots U_{k+1}H_cU_k\cdots U_0$, valid to first order in Δt. Here U needs only to be locally equivalent to a CNOT, and so we modify GRAPE to minimize a cost function C given by the difference between the Makhlin invariants of U and CNOT:

$$C = |G_1|^2 + |G_2 - 1|^2. \tag{27}$$

We note that GRAPE has already been successfully employed in spin-qubit experiments [10].

Although GRAPE is certainly a useful algorithm, it does have limitations. Like any gradient-based optimization algorithm, GRAPE will find a locally optimal solution, but it will typically not find a globally optimal solution if the initial pulse is not close to the global optimum. Additionally, in practice, the locally optimal pulses found by GRAPE often have undesirable properties for experimental implementation, such as being discontinuous, having high bandwidth, starting and/or ending at nonzero values, or changing signs. They can be mitigated to a large extent by starting from an initial pulse that is already close to the global optimum.

Figure 2 shows the result of GRAPE optimization starting from the pulse shown in Fig. 1. The optimized pulses, shown in magenta, are very close to the original pulses, and still quite smooth, but the infidelities after optimization have dropped by about a factor of 5: from 2.51×10^{-3} to 5.37×10^{-4} for the short pulse [Fig. 2(a)], and from 6.82×10^{-3} to 1.65×10^{-3} for the long pulse [Fig. 2(b)].

To showcase the power of the SCQC formalism as a starting point in optimal control, we compare the control pulses obtained in this way to those from the method introduced in Ref. [55] for obtaining low-bandwidth control pulses, where the pulse is represented as a linear combination of bandwidth-constrained

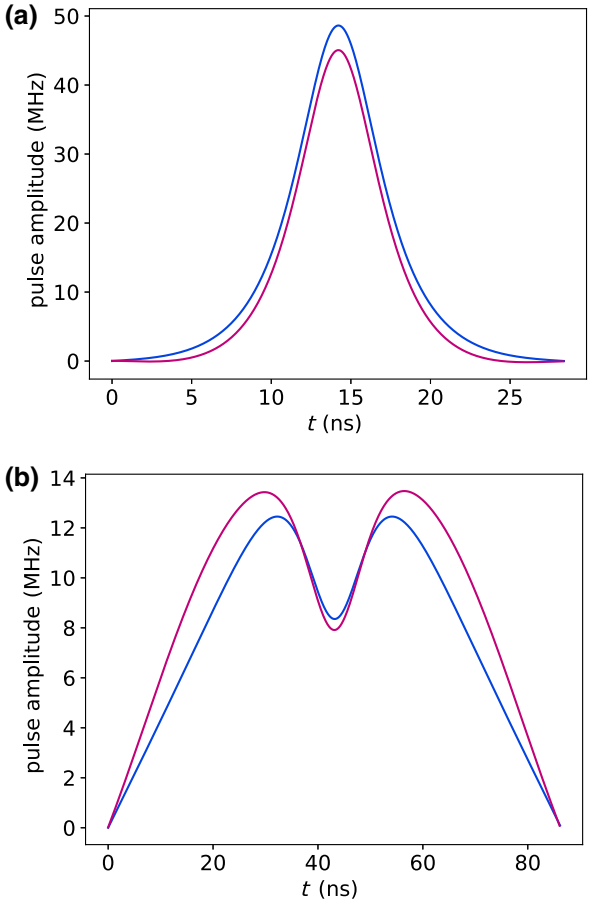

FIG. 2. The initial geometrically designed pulses (blue) shown in Fig. 1, and the GRAPE-optimized pulses (magenta). (a) Faster, higher-amplitude pulses. The initial pulse (blue) has infidelity 2.51×10^{-3}, while the GRAPE-optimized pulse (magenta) has infidelity 5.37×10^{-4}. (b) Slower, lower-amplitude pulses. The initial pulse (blue) has infidelity 6.82×10^{-3}, while the GRAPE-optimized pulse (magenta) has infidelity 1.65×10^{-3}.

Slepian sequences [56]. In this work, we consider Slepian sequences with two different bandwidths for each gate duration: high-bandwidth Slepian sequences with standardized half-bandwidth $NW = 50$, and low-bandwidth Slepian sequences with $NW = 5$. Figure 3 shows a comparison of pulses obtained starting from a geometric pulse, a high-bandwidth Slepian pulse, and a low-bandwidth Slepian pulse. For the 28.4-ns pulses [Fig. 3(a)], the geometric pulse gives an infidelity of 5.37×10^{-4}, while the high- and low-bandwidth Slepian pulses only achieve an infidelity of 3.53×10^{-3} and 4.32×10^{-3}, respectively. For the 86.2-ns pulses [Fig. 3(b)], the geometric pulse gives an infidelity of 1.65×10^{-3}, while the high- and low-bandwidth Slepian pulses achieve infidelities of 3.31×10^{-3} and 1.59×10^{-3}, respectively. Thus we see that, in terms of fidelity, the optimized geometric pulses perform similarly to (if not better than) pulses obtained from Slepian sequences while yielding dramatically simpler (and thus easier to implement in the lab) pulse shapes.

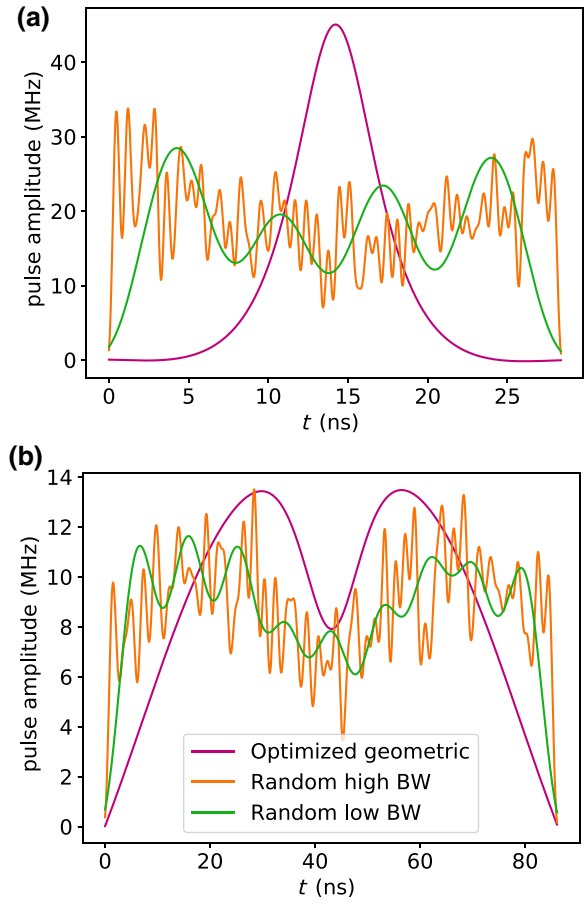

FIG. 3. Comparison of pulses obtained from GRAPE starting from a geometric pulse (blue), and random Slepian pulses with high (orange) and low (green) bandwidth. (a) Faster, higher-amplitude pulses. The high- and low-bandwidth Slepian pulses achieve infidelities of 3.53×10^{-3} and 4.32×10^{-3}, respectively. These should be compared to an infidelity of 5.37×10^{-4} for the GRAPE-optimized geometric pulse (magenta). (b) Slower, lower-amplitude pulses. The high- and low-bandwidth Slepian pulses achieve infidelities of 3.31×10^{-3} and 1.59×10^{-3}, respectively. These should be compared to an infidelity of 1.65×10^{-3} for the GRAPE-optimized geometric pulse (magenta).

B. CRAB

Another example of a robust and widely used numerical optimal control algorithm is the CRAB method [8,12,13]. CRAB expands the driving pulse into a linear combination of predetermined basis functions. To limit the number of basis functions and hence the number of optimization parameters involved, the expansion is normally truncated after a small number of terms. The range of waveforms and gate operations that can be reached with this truncated form can be enhanced by randomizing the choice of the basis. For example, if one takes Fourier components as the basis functions, small random shifts can be added to the normal mode frequencies of the functions to achieve this. In one version of CRAB, one starts from an initial guess for the pulse, expands it into a chosen set of basis functions $g_k(t)$, and then further optimizes the coefficient parameters a_k in the expansion:

$$\Omega_{\mathrm{CRAB}}(t) = \sum_k a_k g_k(t). \tag{28}$$

This approach is most effective if one is able to choose an initial pulse that can be readily expanded in terms of a small number of basis functions. A second approach is to instead modulate the initial pulse $\Omega_0(t)$ using a linear combination of basis functions $f_k(t)$ with coefficients c_k:

$$\Omega_{\mathrm{CRAB}}(t) = \Omega_0(t)\left(1 + \sum_k c_k f_k(t)\right). \tag{29}$$

Here, we employ both versions of CRAB, and we choose Slepian pulses as the basis functions as they are highly

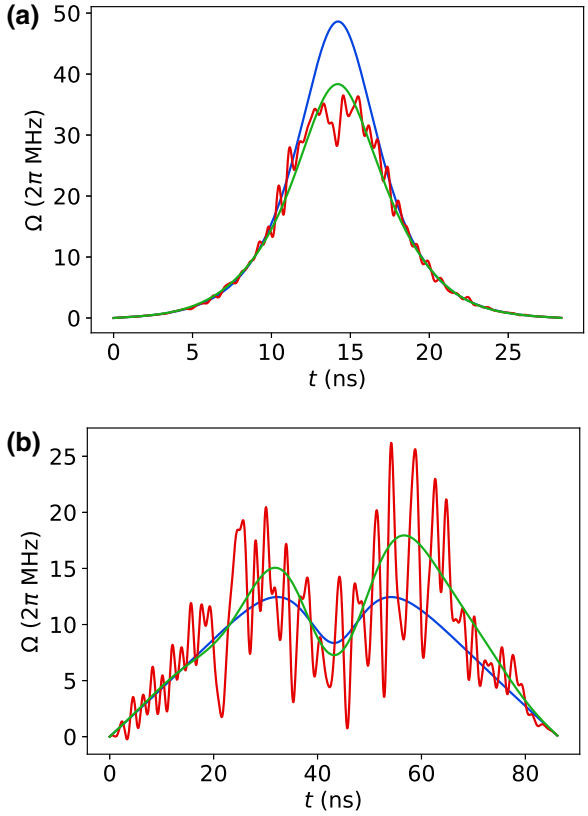

FIG. 4. The initial geometrically designed pulses (blue) shown in Fig. 1 and the CRAB-optimized pulses with low bandwidth (green) and high bandwidth (red). (a) Faster, higher-amplitude pulses. The infidelities of the CRAB-optimized pulses are 2.96×10^{-5} (high bandwidth) and 1.03×10^{-4} (low bandwidth), respectively. (b) Slower, lower-amplitude pulses. The infidelities of the CRAB-optimized pulses are 3.38×10^{-3} (high bandwidth) and 4.15×10^{-4} (low bandwidth), respectively. In both panels, the higher-bandwidth CRAB-optimized pulses (red) are obtained using 96 Slepian basis functions, while the lower-bandwidth pulses (green) use eight Slepian basis functions.

concentrated in both the temporal and frequency domains. As in the previous section, we compare our geometrically designed initial pulses to initial Slepian pulses. In the case of random initial Slepian pulses, we optimize over the Slepian coefficients as in Eq. (28). For geometrically designed initial pulses, we use the second version of CRAB, Eq. (29), as our geometric pulses cannot be easily expanded using a finite set of Slepian functions. As before, we use the two Makhlin invariants as the cost functions for the numerical optimization.

To illustrate the relevance of a good initial pulse, we use our geometrically designed pulses as initial guesses in CRAB. The results are shown in Fig. 4, where we see that, even without imposing any constraints, the CRAB-optimized pulses remain close to the original geometric pulses, which are simple waveforms that are easy to implement experimentally. We see that CRAB reduces the infidelity by an order of magnitude or more (depending on the bandwidth of the Slepian basis that is used) for both the faster (28.4-ns) and slower (86.2-ns) pulses. These improvements are significantly better than those afforded by GRAPE. When a low-bandwidth Slepian basis is used, these improvements are obtained using only eight basis functions. This low overhead is consistent with a general theorem about the number of control parameters needed to reach target states or unitaries [57].

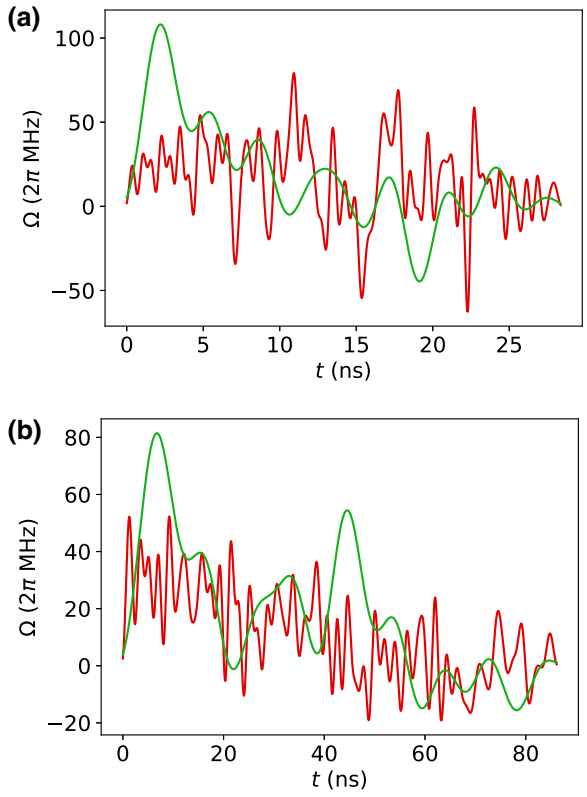

FIG. 5. CRAB-optimized pulses obtained by starting from random Slepian initial pulses with low bandwidth (green) and high bandwidth (red). (a) Faster, higher-amplitude CRAB-optimized pulses. The infidelities are 5.28×10^{-3} (high bandwidth) and 8.14×10^{-4} (low bandwidth), respectively. (b) Slower, lower-amplitude CRAB-optimized pulses. The infidelities are 8.63×10^{-3} (high bandwidth) and 1.93×10^{-3} (low bandwidth), respectively. In both panels, the higher-bandwidth CRAB-optimized pulses (red) are obtained using 96 Slepian basis functions, while the lower-bandwidth pulses (green) use eight Slepian basis functions.

For comparison, we also consider random Slepian pulses as initial pulses in CRAB, with the results shown in Fig. 5. The CRAB-optimized Slepian pulses generally have more complicated shapes and lower fidelities compared to those optimized starting from geometrically designed initial pulses. One could consider imposing additional constraints to further improve the CRAB-optimized results. However, such constraints could possibly introduce additional local minima or false traps in the optimization landscape, and modifications to CRAB have been proposed to overcome this problem [12]. Here, the use of a geometrically designed initial pulse can be viewed as a shortcut to imposing constraints on the numerical algorithm. We see that even when bandwidth constraints are built directly into the basis functions, as is the case when using Slepians, employing SCQC to inject global information about the control landscape into the initial condition for CRAB yields substantially simpler, lower-bandwidth waveforms.

V. CONCLUSION

We introduce a geometrical approach for designing entangling gates that provides a global view of the optimal control landscape by mapping entanglement growth to geometric space curves. We illustrate the method by designing high-fidelity maximally entangling gates for silicon quantum dot spin qubits. We derive the minimal constraints on the space curves needed to guarantee the resulting gates have the desired entangling power. The pulses extracted from the geometric properties of these curves are smooth, have low bandwidth, and start and end at zero amplitude by design, making them experimentally feasible. We show that these pulses can be further improved by GRAPE or CRAB optimization to obtain higher-fidelity operations while keeping the nice properties of the pulses. Our work illustrates how the performance of numerical pulse optimization techniques can be further enhanced by exploiting global information about the optimal control landscape afforded by the geometrical perspective.

ACKNOWLEDGMENTS

This work is supported by the Army Research Office (Grants No. W911NF-15-1-0149 and No. W911NF-17-0287). This work is also supported by the Office of Naval Research (Grant No. N00014-21-1-2629).

APPENDIX: HIGHER-ORDER TERMS IN THE MAGNUS EXPANSION

Here, we derive an expression for the Makhlin invariants in terms of the space curve $\vec{R}$ that includes corrections from the second-order term in the Magnus expansion. Denoting $U_0^\dagger Z Z U_0$ as $Z \otimes \left(\dot{\vec{R}} \cdot \vec{\sigma}_2\right)$, $\tilde{U}$ reads as

$$\tilde{U} \approx \exp\left[-i\frac{J}{4} Z \otimes \left(\vec{R}(t) \cdot \vec{\sigma}_2\right) - i\left(\frac{J}{4}\right)^2 \int_0^t dt_1 I \otimes \left(\dot{\vec{R}}(t_1) \times \vec{R}(t_1)\right) \cdot \vec{\sigma}_2\right].$$

The second term in the exponent is proportional to the area swept by $\vec{R}(t)$. To calculate the Makhlin invariants, we need to calculate the trace of m:

$$\begin{aligned} \mathrm{Tr}(m) &= \mathrm{Tr}[Q^T \tilde{U}^T Q^* Q^\dagger \tilde{U} Q] \\ &= \mathrm{Tr}[Q Q^T \tilde{U}^T Q^* Q^\dagger \tilde{U}] \\ &= \mathrm{Tr}[YY\tilde{U}^T YY\tilde{U}]. \end{aligned}$$

In this case, since the second term in the exponent in $\tilde{U}$ only involves single-qubit Pauli operators, we obtain

$$YY\tilde{U}^T YY \approx \exp\left[-i\frac{J}{4}\sigma_1^z \otimes \left(\vec{R}(t) \cdot \vec{\sigma}_2\right) + i\left(\frac{J}{4}\right)^2 \int_0^t dt_1 I_1 \otimes \left(\dot{\vec{R}}(t_1) \times \vec{R}(t_1)\right) \cdot \vec{\sigma}_2\right],$$

where the second term has a sign difference relative to that in $\tilde{U}$. If the area swept by the space curve is zero, then the second-order term above goes to zero, bringing us back to the expression obtained from keeping only the first term in the Magnus expansion, i.e., Eq. (6). More generally, the traces of m and m^2 become

$$\begin{aligned} \mathrm{Tr}(m) &= 4\cos\theta_- \cos\theta_+ + 4\left(\frac{J}{4}\right)^2 \frac{\left(\frac{J}{4}\right)^2 |\vec{a}(t)|^2 - \left|\vec{R}(t)\right|^2}{\theta_-\theta_+} \sin\theta_- \sin\theta_+, \\ \mathrm{Tr}(m^2)\left(\frac{\theta_-^2\theta_+^2}{\left(\frac{J}{4}\right)^4}\right) &= 2\Bigg[4\left|\left(\frac{J}{4}\right)\vec{a}\times\vec{R}\right|^2 (2\cos(\theta_- + \theta_+)\cos(\theta_- - \theta_+) - 1) \\ &\quad + 2\left(\left(\frac{J}{4}\right)^2 |\vec{a}(t)|^2 - \left|\vec{R}(t)\right|^2\right) \frac{\theta_-\theta_+}{\left(\frac{J}{4}\right)^2} \sin(2\theta_-)\sin(2\theta_+) \\ &\quad + 2\left(\frac{\theta_-^2\theta_+^2}{\left(\frac{J}{4}\right)^4} - 2\left|\left(\frac{J}{4}\right)\vec{a}\times\vec{R}\right|^2\right)\cos(2\theta_-)\cos(2\theta_+)\Bigg], \end{aligned}$$

with $\theta_\pm = J/4\left|J/(4)\vec{a}(t) \pm \vec{R}(t)\right|$ and $\vec{a} = \int_0^t dt_1 \dot{\vec{R}}(t_1) \times \vec{R}(t_1)$. With these expressions, we can obtain the modified analytic expressions for the Makhlin invariants in terms of $\vec{R}(t)$ and then solve for the desired entangling power.

[1] F. Motzoi, J. M. Gambetta, P. Rebentrost, and F. K. Wilhelm, Simple Pulses for Elimination of Leakage in Weakly Nonlinear Qubits, Phys. Rev. Lett. **103**, 110501 (2009).

[2] J. M. Gambetta, F. Motzoi, S. T. Merkel, and F. K. Wilhelm, Analytic control methods for high-fidelity unitary operations in a weakly nonlinear oscillator, Phys. Rev. A **83**, 012308 (2011).

[3] K. A. Landsman, Y. Wu, P. H. Leung, D. Zhu, N. M. Linke, K. R. Brown, L. Duan, and C. Monroe, Two-qubit entangling gates within arbitrarily long chains of trapped ions, Phys. Rev. A **100**, 022332 (2019).

[4] F. A. Calderon-Vargas, G. S. Barron, X.-H. Deng, A. J. Sigillito, E. Barnes, and S. E. Economou, Fast high-fidelity entangling gates for spin qubits in si double quantum dots, Phys. Rev. B **100**, 035304 (2019).

[5] E. Magesan and J. M. Gambetta, Effective hamiltonian models of the cross-resonance gate, Phys. Rev. A **101**, 052308 (2020).

[6] S. Kirchhoff, T. Keßler, P. J. Liebermann, E. Assémat, S. Machnes, F. Motzoi, and F. K. Wilhelm, Optimized cross-resonance gate for coupled transmon systems, Phys. Rev. A **97**, 042348 (2018).

[7] N. Khaneja, T. Reiss, C. Kehlet, T. Schulte-Herbrüggen, and S. J. Glaser, Optimal control of coupled spin dynamics: design of nmr pulse sequences by gradient ascent algorithms, Journal of Magnetic Resonance **172**, 296 (2005).

[8] T. Caneva, T. Calarco, and S. Montangero, Chopped random-basis quantum optimization, Phys. Rev. A **84**, 022326 (2011).

[9] E. Barnes, C. Arenz, A. Pitchford, and S. E. Economou, Fast microwave-driven three-qubit gates for cavity-coupled superconducting qubits, Phys. Rev. B **96**, 024504 (2017).

[10] C. H. Yang, K. W. Chan, R. Harper, W. Huang, T. Evans, J. C. C. Hwang, B. Hensen, A. Laucht, T. Tanttu, F. E. Hudson, S. T. Flammia, K. M. Itoh, A. Morello, S. D. Bartlett, and A. S. Dzurak, Silicon qubit fidelities approaching incoherent noise limits via pulse engineering, Nature Electronics **2**, 151 (2019).

[11] S. J. Glaser, U. Boscain, T. Calarco, C. P. Koch, W. Köckenberger, R. Kosloff, I. Kuprov, B. Luy, S. Schirmer, T. Schulte-Herbrüggen, D. Sugny, and F. K. Wilhelm, Training Schrödinger's cat: Quantum optimal control, Eur. Phys. J. D **69**, 279 (2015).

[12] M. M. Müller, R. S. Said, F. Jelezko, T. Calarco, and S. Montangero, One decade of quantum optimal control in the chopped random basis, Rep. Prog. Phys. **85**, 076001 (2022).

[13] P. Doria, T. Calarco, and S. Montangero, Optimal Control Technique for Many-Body Quantum Dynamics, Phys. Rev. Lett. **106**, 190501 (2011).

[14] M. Veldhorst, C. H. Yang, J. C. C. Hwang, W. Huang, J. P. Dehollain, J. T. Muhonen, S. Simmons, A. Laucht, F. E. Hudson, K. M. Itoh, A. Morello, and A. S. Dzurak, A two-qubit logic gate in silicon, Nature **526**, 410 (2015).

[15] W. Huang, C. H. Yang, K. W. Chan, T. Tanttu, B. Hensen, R. C. C. Leon, M. A. Fogarty, J. C. C. Hwang, F. E. Hudson, K. M. Itoh, A. Morello, A. Laucht, and A. S. Dzurak, Fidelity benchmarks for two-qubit gates in silicon, Nature **569**, 532 (2019).

[16] X. Xue, M. Russ, N. Samkharadze, B. Undseth, A. Sammak, G. Scappucci, and L. M. K. Vandersypen, Quantum logic with spin qubits crossing the surface code threshold, Nature **601**, 343 (2022).

[17] A. Noiri, K. Takeda, T. Nakajima, T. Kobayashi, A. Sammak, G. Scappucci, and S. Tarucha, Fast universal quantum gate above the fault-tolerance threshold in silicon, Nature **601**, 338 (2022).

[18] A. R. Mills, C. R. Guinn, M. J. Gullans, A. J. Sigillito, M. M. Feldman, E. Nielsen, and J. R. Petta, Two-qubit silicon quantum processor with operation fidelity exceeding 99%, Sci. Adv. **8**, eabn5130 (2022).

[19] R. C. C. Leon, C. H. Yang, J. C. C. Hwang, J. Camirand Lemyre, T. Tanttu, W. Huang, J. Y. Huang, F. E. Hudson, K. M. Itoh, A. Laucht, M. Pioro-Ladrière, A. Saraiva, and A. S. Dzurak, Bell-state tomography in a silicon many-electron artificial molecule, Nat. Commun. **12**, 3228 (2021).

[20] A. E. Seedhouse, T. Tanttu, R. C. Leon, R. Zhao, K. Y. Tan, B. Hensen, F. E. Hudson, K. M. Itoh, J. Yoneda, C. H. Yang, A. Morello, A. Laucht, S. N. Coppersmith, A. Saraiva, and A. S. Dzurak, Pauli Blockade in Silicon Quantum Dots with Spin-Orbit Control, PRX Quantum **2**, 010303 (2021).

[21] R. Barends *et al.*, Superconducting quantum circuits at the surface code threshold for fault tolerance, Nature **508**, 500 (2014).

[22] S. Sheldon, E. Magesan, J. M. Chow, and J. M. Gambetta, Procedure for systematically tuning up cross-talk in the cross-resonance gate, Phys. Rev. A **93**, 060302 (2016).

[23] P. Krantz, M. Kjaergaard, F. Yan, T. P. Orlando, S. Gustavsson, and W. D. Oliver, A quantum engineer's guide to superconducting qubits, Appl. Phys. Rev. **6**, 021318 (2019).

[24] M. A. Rol, F. Battistel, F. K. Malinowski, C. C. Bultink, B. M. Tarasinski, R. Vollmer, N. Haider, N. Muthusubramanian, A. Bruno, B. M. Terhal, and L. DiCarlo, Fast, High-Fidelity Conditional-Phase Gate Exploiting Leakage Interference in Weakly Anharmonic Superconducting Qubits, Phys. Rev. Lett. **123**, 120502 (2019).

[25] Y. Y. Gao, B. J. Lester, K. S. Chou, L. Frunzio, M. H. Devoret, L. Jiang, S. M. Girvin, and R. J. Schoelkopf, Entanglement of bosonic modes through an engineered exchange interaction, Nature **566**, 509 (2019).

[26] L. Egan, D. M. Debroy, C. Noel, A. Risinger, D. Zhu, D. Biswas, M. Newman, M. Li, K. R. Brown, M. Cetina, and C. Monroe, Fault-tolerant control of an error-corrected qubit, Nature **598**, 281 (2021).

[27] R. Srinivas, S. C. Burd, H. M. Knaack, R. T. Sutherland, A. Kwiatkowski, S. Glancy, E. Knill, D. J. Wineland, D. Leibfried, A. C. Wilson, D. T. C. Allcock, and D. H. Slichter, High-fidelity laser-free universal control of trapped ion qubits, Nature **597**, 209 (2021).

[28] I. Pogorelov, T. Feldker, C. D. Marciniak, L. Postler, G. Jacob, O. Krieglsteiner, V. Podlesnic, M. Meth, V. Negnevitsky, M. Stadler, B. Höfer, C. Wächter, K. Lakhmanskiy, R. Blatt, P. Schindler, and T. Monz, Compact Ion-Trap Quantum Computing Demonstrator, PRX Quantum **2**, 020343 (2021).

[29] D. S. Wang, A. G. Fowler, and L. C. L. Hollenberg, Surface code quantum computing with error rates over 1 %, Phys. Rev. A **83**, 020302 (2011).

[30] A. G. Fowler, M. Mariantoni, J. M. Martinis, and A. N. Cleland, Surface codes: Towards practical large-scale quantum computation, Phys. Rev. A **86**, 032324 (2012).

[31] E. Barnes, F. A. Calderon-Vargas, W. Dong, B. Li, J. Zeng, and F. Zhuang, Dynamically corrected gates from geometric space curves, Quantum Sci. Technol. **7**, 023001 (2022).

[32] J. Zeng, X.-H. Deng, A. Russo, and E. Barnes, General solution to inhomogeneous dephasing and smooth pulse dynamical decoupling, New J. Phys. **20**, 033011 (2018).

[33] J. Zeng and E. Barnes, Fastest pulses that implement dynamically corrected single-qubit phase gates, Phys. Rev. A **98**, 012301 (2018).

[34] J. Zeng, C. H. Yang, A. S. Dzurak, and E. Barnes, Geometric formalism for constructing arbitrary single-qubit dynamically corrected gates, Phys. Rev. A **99**, 052321 (2019).

[35] D. Buterakos, S. Das Sarma, and E. Barnes, Geometrical Formalism for Dynamically Corrected Gates in Multiqubit Systems, PRX Quantum **2**, 010341 (2021).

[36] F. Zhuang, J. Zeng, S. E. Economou, and E. Barnes, Noise-resistant Landau-Zener sweeps from geometrical curves, Quantum **6**, 639 (2022).

[37] W. Dong, F. Zhuang, S. E. Economou, and E. Barnes, Doubly Geometric Quantum Control, PRX Quantum **2**, 030333 (2021).

[38] H. T. Nelson, E. Piliouras, K. Connelly, and E. Barnes, Designing dynamically corrected gates robust to multiple noise sources using geometric space curves (2022).

[39] D. Loss and D. P. DiVincenzo, Quantum computation with quantum dots, Phys. Rev. A **57**, 120 (1998).
[40] F. A. Zwanenburg, A. S. Dzurak, A. Morello, M. Y. Simmons, L. C. L. Hollenberg, G. Klimeck, S. Rogge, S. N. Coppersmith, and M. A. Eriksson, Silicon quantum electronics, Rev. Mod. Phys. **85**, 961 (2013).
[41] M. F. Gonzalez-Zalba, S. de Franceschi, E. Charbon, T. Meunier, M. Vinet, and A. S. Dzurak, Scaling silicon-based quantum computing using CMOS technology, Nature Electronics **4**, 872 (2021).
[42] A. M. J. Zwerver *et al.*, Qubits made by advanced semiconductor manufacturing, Nat. Electron. **5**, 184 (2022).
[43] J. Yoneda, K. Takeda, T. Otsuka, T. Nakajima, M. R. Delbecq, G. Allison, T. Honda, T. Kodera, S. Oda, Y. Hoshi, N. Usami, K. M. Itoh, and S. Tarucha, A quantum-dot spin qubit with coherence limited by charge noise and fidelity higher than 99.9%, Nat. Nanotechnol. **13**, 102 (2018).
[44] P. Huang, N. M. Zimmerman, and G. W. Bryant, Spin decoherence in a two-qubit cphase gate: The critical role of tunneling noise, Npj Quantum Inf. **4**, 62 (2018).
[45] J. van Dijk, E. Kawakami, R. Schouten, M. Veldhorst, L. Vandersypen, M. Babaie, E. Charbon, and F. Sebastiano, Impact of Classical Control Electronics on Qubit Fidelity, Phys. Rev. Appl. **12**, 044054 (2019).
[46] K. W. Chan, W. Huang, C. H. Yang, J. C. C. Hwang, B. Hensen, T. Tanttu, F. E. Hudson, K. M. Itoh, A. Laucht, A. Morello, and A. S. Dzurak, Assessment of a Silicon Quantum Dot Spin Qubit Environment via Noise Spectroscopy, Phys. Rev. Appl. **10**, 044017 (2018).
[47] K. M. Itoh and H. Watanabe, Isotope engineering of silicon and diamond for quantum computing and sensing applications, MRS Commun. **4**, 143 (2014).
[48] K. C. Nowack, F. H. L. Koppens, Y. V. Nazarov, and L. M. K. Vandersypen, Coherent control of a single electron spin with electric fields, Science **318**, 1430 (2007).
[49] F. Martins, F. K. Malinowski, P. D. Nissen, E. Barnes, S. Fallahi, G. C. Gardner, M. J. Manfra, C. M. Marcus, and F. Kuemmeth, Noise Suppression using Symmetric Exchange Gates in Spin Qubits, Phys. Rev. Lett. **116**, 116801 (2016).
[50] M. D. Reed, B. M. Maune, R. W. Andrews, M. G. Borselli, K. Eng, M. P. Jura, A. A. Kiselev, T. D. Ladd, S. T. Merkel, I. Milosavljevic, E. J. Pritchett, M. T. Rakher, R. S. Ross, A. E. Schmitz, A. Smith, J. A. Wright, M. F. Gyure, and A. T. Hunter, Reduced Sensitivity to Charge Noise in Semiconductor Spin Qubits via Symmetric Operation, Phys. Rev. Lett. **116**, 110402 (2016).
[51] D. M. Zajac, A. J. Sigillito, M. Russ, F. Borjans, J. M. Taylor, G. Burkard, and J. R. Petta, Resonantly driven CNOT gate for electron spins, Science **359**, 439 (2018).
[52] Y. Makhlin, Nonlocal properties of two-qubit gates and mixed states, and the optimization of quantum computations, Quantum Inf. Process. **1**, 243 (2002).
[53] R. F. Hartl, S. P. Sethi, and R. G. Vickson, A survey of the maximum principles for optimal control problems with state constraints, SIAM Review **37**, 181 (1995).
[54] N. Wittler, F. Roy, K. Pack, M. Werninghaus, A. S. Roy, D. J. Egger, S. Filipp, F. K. Wilhelm, and S. Machnes, Integrated Tool Set for Control, Calibration, and Characterization of Quantum Devices Applied to Superconducting Qubits, Phys. Rev. Appl. **15**, 034080 (2021).
[55] D. Lucarelli, Quantum optimal control via gradient ascent in function space and the time-bandwidth quantum speed limit, Phys. Rev. A **97**, 062346 (2018).
[56] D. Slepian, Prolate spheroidal wave functions, Fourier analysis, and uncertainty—V: The discrete case, Bell Syst. Tech. J. **57**, 1371 (1978).
[57] S. Lloyd and S. Montangero, Information Theoretical Analysis of Quantum Optimal Control, Phys. Rev. Lett. **113**, 010502 (2014).